Longitudinal sound velocities, elastic anisotropy, and phase transition of high-pressure cubic H_2O ice to 82 GPa

Maju Kuriakose,[1] Samuel Raetz,[1] Qing Miao Hu,[2] Sergey M. Nikitin,[1] Nikolay Chigarev,[1] Vincent Tournat,[1] Alain Bulou,[3] Alexey Lomonosov,[4] Philippe Djemia,[5] Vitalyi E. Gusev,[1,*] and Andreas Zerr[5,*]

[1]*Laboratoire d'Acoustique de l'Université du Maine (LAUM), UMR-CNRS 6613, Université du Maine, Avenue Olivier Messiaen, 72085 Le Mans, France*

[2]*Institute of Metal Research, Chinese Academy of Sciences, Shenyang 110016, China*

[3]*Institut des Molécules et Matériaux du Mans (IMMM), UMR-CNRS 6283, Université du Maine, Avenue Olivier Messiaen, 72085 Le Mans, France*

[4]*Prokhorov General Physics Institute, Russian Academy of Sciences, 119991 Moscow, Russian Federation*

[5]*Laboratoire des Sciences des Procédés et des Matériaux (LSPM), UPR-CNRS 3407, Université Paris Nord, Avenue J. B. Clément, 93430 Villetaneuse, France*

(Received 30 September 2016; revised manuscript received 15 October 2017; published 30 October 2017)

Water ice is a molecular solid whose behavior under compression reveals the interplay of covalent bonding in molecules and forces acting between them. This interplay determines high-pressure phase transitions, the elastic and plastic behavior of H_2O ice, which are the properties needed for modeling the convection and internal structure of the giant planets and moons of the solar system as well as H_2O-rich exoplanets. We investigated experimentally and theoretically elastic properties and phase transitions of cubic H_2O ice at room temperature and high pressures between 10 and 82 GPa. The time-domain Brillouin scattering (TDBS) technique was used to measure longitudinal sound velocities (V_L) in polycrystalline ice samples compressed in a diamond anvil cell. The high spatial resolution of the TDBS technique revealed variations of V_L caused by elastic anisotropy, allowing us to reliably determine the fastest and the slowest sound velocity in a single crystal of cubic H_2O ice and thus to evaluate existing equations of state. Pressure dependencies of the single-crystal elastic moduli $C_{ij}(P)$ of cubic H_2O ice to 82 GPa have been obtained which indicate its hardness and brittleness. These results were compared with *ab initio* calculations. It is suggested that the transition from molecular ice VII to ionic ice X occurs at much higher pressures than proposed earlier, probably above 80 GPa.

DOI: 10.1103/PhysRevB.96.134122

I. INTRODUCTION

H_2O is one of the most abundant compounds appearing in all aggregate states in the universe [1–3]. Mainly it is accumulated as solid ice subjected to high pressure (HP) in the interiors of the outer planets of the solar system such as Uranus and Neptune or the satellites of Jupiter and Saturn [2,4,5] and in H_2O-rich exoplanets [6,7]. In order to model the internal structure and compositional differentiation of these planets applying gravitational observations, pressure dependencies of densities and of elastic moduli of the constituting compounds are required [1,6,7]. Interplay of inter- and intramolecular bonding in H_2O ice upon compression leads to a complex *P-T* phase diagram with strongly changing elastic behavior of the ice phases. Moreover, the molecular nature of H_2O is expected to disappear at very high pressures [8–10].

Solid H_2O is known to crystallize in 14 different polymorphs in which the molecules build crystal lattices [2,9,10]. All but two molecular phases are confined to a narrow pressure interval below ∼2.5 GPa. Above this pressure H_2O ice assumes, at room temperature, a cubic structure with disordered H_2O molecules [11,12]. This cubic ice VII phase (with proton positions much more strongly disordered than those of oxygen) transforms below 278 K [2,10,13] into ice VIII having a closely related tetragonal structure with ordered proton positions [11,14]. It has been proposed in the literature that the molecular nature of ice VII and VIII vanishes upon compression due to shifting of protons to the symmetric positions, halfway between the oxygen anions, and another ionic form of ice, named ice X, appears [8,15–18]. However, the transition pressure has remained controversial with values between 40 and 100 GPa [8,10,12,15,16,19,20]. Moreover, transitions to intermediate phases such as a tetragonally distorted ice VII above 14 GPa [21], "ionized" ice VII above 55 GPa [16], or a phase with protons occupying octahedral interstitials of the O sublattice [22] were suggested to explain the controversial structural observations from neutron and x-ray diffraction (XRD) studies. Measurements of the refractive index of H_2O ice to 120 GPa showed a systematic shift with pressure but slight changes in $n(P)$ were recognized at 40, 60, and 90 GPa [20]. In the pressure region from 60 to 90 GPa, ice VII was supposed to evolve into symmetric ice X but no explanation for the kink in $n(P)$ at 40 GPa was proposed [20].

None of the existing high-pressure XRD measurements on ice VII and ice X, where intensities of the diffraction patterns are dominated by x-ray scattering from the O sublattice, detected a jump in the equation of state (EOS), $\rho(P)$ [19,23–25]. This implies a negligible hysteresis of the phase transition; e.g., the transition from ice VII to ice X upon compression and the reverse one upon decompression should occur at the same pressure. Also, coexistence of the two phases is expected to be confined to a very narrow pressure range. An extended two-phase pressure region could artificially appear in the experiments where lateral pressure

*Corresponding authors: vitali.goussev@univ-lemans.fr; zerr@univ-paris13.fr

variations in the sample areas illuminated with probing x rays are significant. Because H_2O ice is a weak scatterer of x rays, sample irradiation with expanded beams was the only way to obtain signals of acceptable quality, especially at pressures approaching 100 GPa where the samples are thin. This could explain why in some publications there are kinks in the measured pressure dependencies of $\rho(P)$ comparable to or exceeding the experimental uncertainties [24,25]. Nevertheless, most of the high-pressure XRD studies provided a single $\rho(P)$ to describe compressibility of the both cubic ice phases [17,19,23,24,26]. The reported $\rho(P)$ and, accordingly, bulk moduli, $B(P) = \rho(\partial P/\partial\rho)_T$, evince, however, substantial differences exceeding 20% at ~60 GPa [17,27]. Apart from pressure gradients, possible reasons for these differences could be a significant yield stress of the cubic H_2O ice combined with a large elastic anisotropy strongly biasing the interplanar distances for different crystallographic orientations [19,21,23,24]. Quality of the XRD data could not be improved by using quasihydrostatic pressure media such as He or Ne because embedding of ice samples in these media led to formation of clathrates or intercalation of the inert gas atoms into the ice structure [21].

So far, no convincing criterion to confirm an EOS measured using the XRD technique has been proposed. Attempts to determine an EOS of the cubic H_2O ice applying optical interference patterns in an H_2O ice sample compressed in a diamond anvil cell (DAC) did not clarify the situation as well: Zha *et al.* [20] reported pressure dependence of the thickness of a compressed H_2O ice sample $h(P)$ using their own refractive index $n(P)$ and compared the obtained dependence $h(P)/h_0$ with a selection of earlier $\rho(P)$ from the XRD measurements. Unfortunately, their experimental data points $h(P)/h_0$ scattered much stronger than the selected $\rho(P)$. This result was biased by a loss of the circular shape of the sample and considered to provide only qualitative insight so that no independent EOS could be deduced. A limited reliability of the available experimental equations of state of the cubic H_2O ice led to an important consequence for the theory: Theorists miss an experimental reference by comparison of the theoretical equations of state calculated using different functionals describing the O-H interaction [17]. Absence of the most appropriate functional prohibits further progress in *ab initio* studies of H_2O ice, including the cubic phases.

A significant elastic anisotropy of the cubic H_2O ice was recognized in some XRD experiments, however, without any reliable quantification [19,21,23,24]. Frequency-domain Brillouin scattering (FDBS), conducted on single crystals of ice VII compressed in a DAC up to 8 GPa, showed a strong dependence of the longitudinal and transversal sound velocities, V_L and V_T, on crystallographic orientations resulting in the anisotropy factor $A = 2C_{44}/(C_{11} - C_{12}) = 3$ at the highest pressure [28]. The maximum and minimum longitudinal sound velocities, $V_{L\max}$ and $V_{L\min}$, correspond in cubic single crystals to the velocities along the crystallographic directions ⟨111⟩ and ⟨100⟩, respectively, as given by the expressions $V_{L\langle111\rangle} = (C^*/\rho)^{1/2} = [(C_{11} + 2C_{12} + 4C_{44})/3\rho]^{1/2}$ and $V_{L\langle100\rangle} = (C_{11}/\rho)^{1/2}$. For single crystals of ice VII compressed to $P = 8$ GPa, Shimizu *et al.* [28] reported $V_{L\max} = V_{L\langle111\rangle} = 7.82$ km/s and $V_{L\min} = V_{L\langle100\rangle} = 6.30$ km/s (Fig. 1).

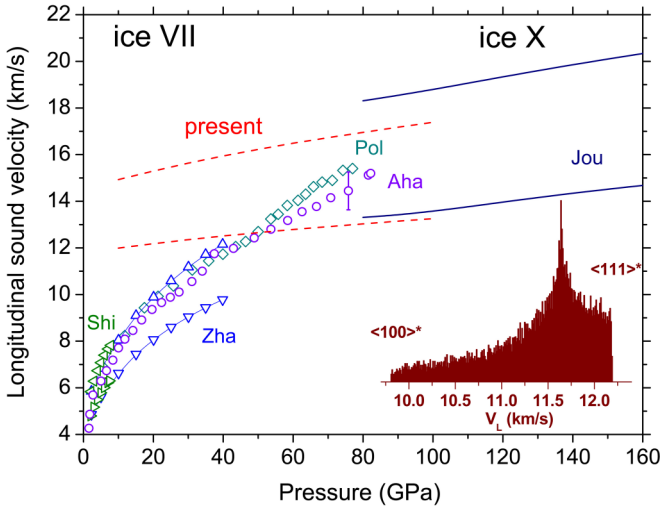

FIG. 1. Earlier data on $V_L(P)$ of ice VII and ice X at high pressures. Symbols represent experimental data from classical FDBS measurements: Open green triangles pointing left and right are $V_{L\langle111\rangle}(P)$ and $V_{L\langle100\rangle}(P)$, respectively, obtained for single crystals of ice VII by Shimizu *et al.* [28]; open blue triangles pointing up and down are $V_{L\langle111\rangle}(P)$ and $V_{L\langle100\rangle}(P)$, respectively, calculated from the $C_{ij}(P)$ dependencies reported by Zha *et al.* [30]; diamonds and circles are longitudinal sound velocities $V_{L\mathrm{av}}(P)$ derived from averaged FDBS spectra of polycrystalline ice samples by Polian and Grimsditch [26] and Ahart *et al.* [29], respectively. The error bar shows the full width at half maximum (FWHM) of the FDBS peak at 77 GPa shown in the latter work. Lines represent theoretical $V_{L\langle111\rangle}(P)$ and $V_{L\langle100\rangle}(P)$ calculated for ice X: solid lines, earlier results of Journaux *et al.* [3]; dashed lines, our *ab initio* calculations. The inset shows orientational distribution of V_L in a single crystal of ice VII calculated using the C_{ij} values at 40 GPa reported by Zha *et al.* [30]. This distribution is equivalent to the statistical distribution of sound velocities in grains of a texture-free polycrystalline sample along a selected spatial direction and depicts the ideal shape of an averaged FDBS spectrum collected for such a sample. Directions of the fastest and the slowest sound propagation in the cubic ice crystal are ⟨111⟩ and ⟨100⟩, respectively. The star indicates that the C_{ij} values were obtained using the envelope method and are consequently approximate. The distribution has a maximum at 11.64 km/s and its center of mass (corresponds to the most probable velocity) is located at 11.56 km/s. For a texture-free sample with B and G calculated using the same C_{ij} values applying the Voigt approximation we obtained $V_L = 11.26$ km/s. This value deviates from the most probable velocity by 13% of the difference between the fastest and the slowest velocities in a single crystal. Applying the Voigt-Reuss-Hill approximation to determine G of the same polycrystalline sample we obtained $V_L = 10.92$ km/s which deviates even stronger from the most probable velocity, namely by 27%.

Even though single crystals of ice VII disintegrate into polycrystalline domains upon further compression in a DAC [19,23,29,30], multiple resolved FDBS peaks with varying frequencies have been observed by scanning over such samples. This observation was explained by varying orientation of elastically anisotropic ice grains upon scanning and used to construct $C_{ij}(P)$ of ice VII to 40 GPa by applying the so-called envelope method [29,30]: At each selected pressure, the FDBS peak giving the maximal V_L is attributed to the crystallographic direction ⟨111⟩ while that giving the minimal

V_L to the direction ⟨100⟩. However, at pressures below 10 GPa this approach led to a smaller value of $A = 2.4$ when compared with the single-crystal data in Ref. [28]. This indicated a limited applicability of the envelope method by examination of polycrystalline samples using the classical FDBS. Independent FDBS studies on polycrystalline samples reported only averaged sound velocities $V_{L\,\mathrm{av}}(P)$ and $V_{T\,\mathrm{av}}(P)$ to ∼80 GPa [26,29]. A remarkable tendency of $V_{L\,\mathrm{av}}(P)$ to approach $V_{L\,\mathrm{max}}(P)$ (Fig. 1) was yet neither recognized nor discussed in the literature. As we show below, this is due to a large elastic anisotropy of cubic ice VII. Furthermore, there is an astonishing contradiction between the claimed phase transition to ice X at 40–60 GPa and absence of a jump of $V_{L\,\mathrm{av}}$ (which should approach $V_{L\,\mathrm{max}}$) upon this transition in the reported classical FDBS measurements [26,29]. Such a jump is required by the recent theoretical calculations of $C_{ij}(P)$ of ice X predicting at 40–60 GPa much higher $V_{L\,\mathrm{max}}(P)$ for this phase than for ice VII [3] (see Fig. 1). The jump had to be observed in the classical FDBS measurements on *polycrystalline texture-free* samples of cubic H_2O ice because of the following two reasons: (i) the transition from phase VII to phase X is hysteresis-free and (ii) pressure variations along the sample depth are negligibly small (see below for more details). Accordingly, the sample volume irradiated with a laser (throughout the whole sample depth) in the classical FDBS measurements had to be either ice VII or ice X, provided the lateral pressure gradients within the irradiated sample area are negligible. As already emphasized above, two phases can be detected at the same pressure only if the phase transition exhibits a significant hysteresis, proportional to the density jump associated with the transition. It is to be recalled that in all the existing XRD measurements no density jump upon the transition from ice VII to ice X has been reported. Accordingly, experimental information on $V_{L\,\mathrm{max}}$ and $V_{L\,\mathrm{min}}$ of cubic H_2O ice at $P > 40$ GPa is the key to clarification of the recognized contradiction.

These considerations show that even in the case of a solid having cubic structure its elastic anisotropy can strongly bias the quality of the data obtained using XRD and classical FDBS, especially for samples under nonhydrostatic load. These two techniques deliver better results for single crystals compressed quasihydrostatically and were applied for establishing the primary pressure scale, a central problem of the condensed matter physics. However, the maximal achieved pressures remained below 60 GPa and the results reported by different groups deviate [31–33]. In addition to the nonhydrostatic loading and to the elastic anisotropy, the classical FDBS data are known to be sensitive to the experiment geometry which can introduce systematic errors [33]. Since quasihydrostatic loading conditions and persistence of single crystals cannot be expected at pressures above 100 GPa [34], other methods suitable for establishing a reliable primary pressure scale should be considered. Our results demonstrate that the here applied time-domain Brillouin scattering (TDBS) having a high spatial resolution [35,36] provides the needed performance.

II. METHODS

A. High-pressure technique

Samples of H_2O ice studied here between 10 and 82 GPa were compressed in a Boehler-Almax Plate DAC [37] with diamond anvils having culets of 300 μm in diameter. They were prepared by filling a hole in a preindented stainless steel gasket with distilled water which solidifies at room temperature above ∼1 GPa. The samples had an initial diameter of about 100 μm and thickness of <30 μm and contained thin iron disks of ∼2 μm in thickness and <70 μm in diameter sticking to the culet of one of the anvils. The disk served as the optoacoustic generator of coherent acoustic pulses launched into and propagating through the ice sample (see below). It was produced prior to filling the sample volume with water by squashing a small iron sphere between the anvil culets and thus had a similarly high surface quality to that of the culets. The generator thickness was estimated from the difference of the water ice thickness in two neighbor positions, above and near the generator. The latter values were obtained using the optical interference method [20,38]. We note that thickness of neither the generator nor the ice sample was needed in our TDBS measurements because these values are not required for the signal treatment (see below). Finally, a few ruby grains were distributed around the optoacoustic generator for the pressure measurement via the calibrated shift of the $R1$ fluorescence line [39]. Broadening of the $R1$ and $R2$ fluorescence lines of ruby was recognized upon load increase but the lines were clearly separated up to the highest pressure of the work.

The ice samples, obtained by solidification of water upon compression, were first brought to the maximal pressure of 57 GPa or of 82 GPa, then gradually decompressed and the TDBS signals collected, as outlined below. This procedure assured the same high degree of polycrystallinity of the samples on pressure change. Texture-free polycrystalline H_2O ice samples cannot be obtained on pressure increase because large crystals having specific orientations with respect to the anvil culets form by solidification of water. These large ice crystals disintegrate upon further compression but samples become nearly texture-free at relatively high pressures, in excess of 20–30 GPa [22,23]. Our TDBS measurements could not provide in this case statistically reliable information about V_L values for all possible orientations in a single crystal of H_2O ice because sound velocities were measured for only one propagation direction, along the sample depth. In this work we performed two sets of measurements: In the first one, the starting maximal pressure was 57 GPa, the sample thickness was 14.4 μm, and the optoacoustic generator diameter was 66 μm. In the second one, the starting maximal pressure was 82 GPa, the sample thickness was 13.5 μm, and the generator diameter was 40 μm [35].

B. TDBS technique

To obtain reliable values of the longitudinal sound velocities and information about their spatial variations in a sample of cubic H_2O ice under compression, we applied the TDBS technique recently adapted to transparent samples subjected to Mbar pressures in a DAC [35,36]. The technique is based on a coherent phonon generation and detection by picosecond laser pulses [40]. In our setup, described in detail elsewhere [35,36], a pulsed Ti:sapphire laser (Spectra-Physics, 2 W, $\lambda_L = 808$ nm, 2.7 ps pulse width) was used. Its radiation was split into two beams and the frequency of one of them was

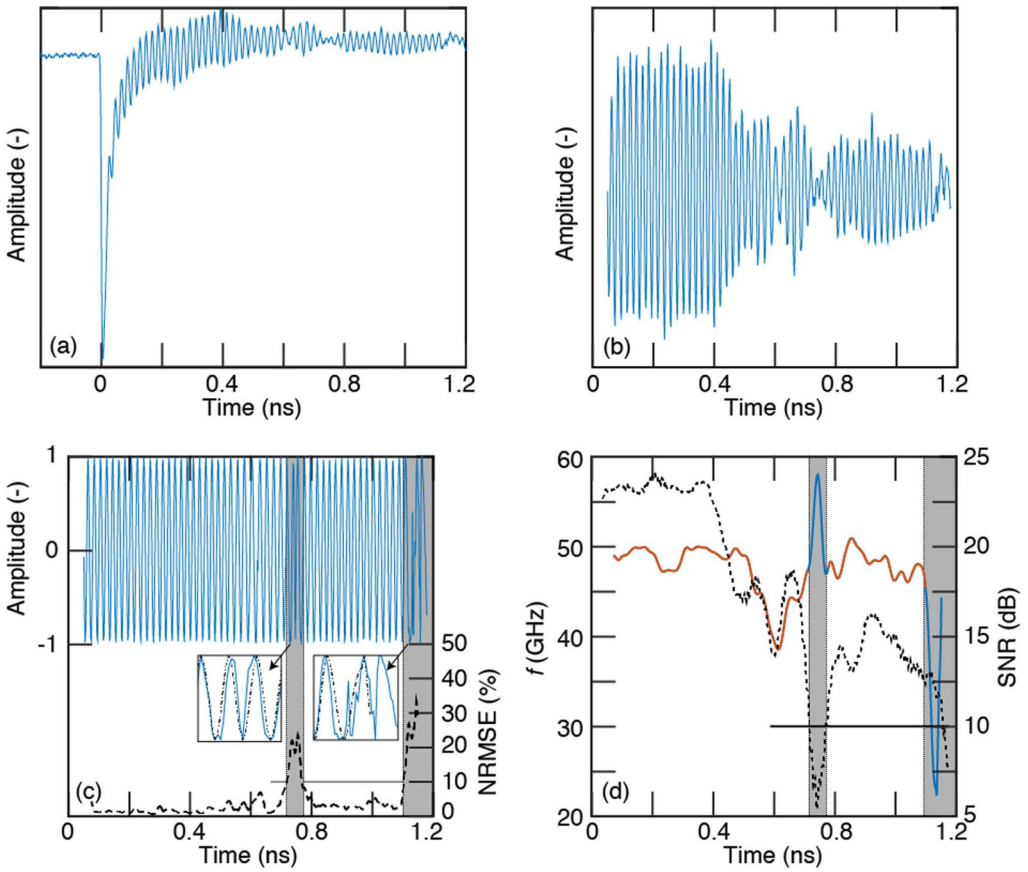

FIG. 2. Processing of a TDBS signal collected from an H_2O ice sample compressed in a DAC to 33 GPa. (a) Raw transient reflectivity signal $S(t)$. (b) Corresponding filtered signal $s(t)$ where the nonoscillating background, caused by a transient heating of the sample, was removed. Here, both amplitude and the phase change with time: $A(t)\cos[\phi(t)]$. (c) The amplitude-variation-free signal $\cos[\phi(t)]$ (solid blue line) and normalized root-mean-square error (NRMSE) between the windowed complex exponential $\exp[j\,\phi(t)]$ and the corresponding extracted complex exponential (dashed black line). The insets show, with a higher magnification, the time segments indicated by the gray background where the signals (blue solid lines) deviate significantly from the best fit by the harmonic function (dashed-dotted lines). These time segments were excluded from further consideration due to a large NRMSE exceeding 10%. (d) Instantaneous signal frequency derived using the synchronous detection technique (solid red line) and the SNR (dashed black line). Gray background in (d) indicates time segments with a poor SNR (smaller than 10 dB) and/or with a large NRMSE (greater than 10%).

doubled ($\lambda = 404$ nm, 1.9 ps pulse width). The latter beam was focused on the optically absorbing optoacoustic generator (a thin iron disk) which lunched, due to subsequent transient heating and expansion, ultrashort acoustic pulses into the ice sample. Even though the transient heating of the optoacoustic generator did not exceed 3 °C [41], its expansion produced a significantly strong density perturbation within the acoustic pulse permitting a reliable detection of its propagation through the transparent ice sample. For this purpose we used the time-delayed pulses of the second beam with $\lambda_L = 808$ nm. Interference of reflections of this probe beam from different stationary surfaces/interfaces in the DAC and from the moving photogenerated acoustic pulse, due to the acousto-optic effect, resulted in an oscillating signal $S(t)$ (Fig. 2) recorded using a photodetector. At each instant of time t, the signal frequency $f(t)$ is related to the velocity of the longitudinal acoustic wave V_L at the position where the laser-generated picosecond acoustic pulse is located during its propagation through the sample depth. No indication of a contribution of transversal acoustic waves was recognized in the collected signals. The lateral resolution of our TDBS measurement of 4.5 μm was defined by focusing of the pump and probe beams while the in-depth resolution of $<0.1\mu$m was limited by the width of the acoustic pulse [35]. Frequency of the collected TDBS signal (and its variations with depth due to elastic anisotropy of the sample material) (Fig. 2) was converted into longitudinal sound velocity (and its variations) applying the classical formula $V_L(P) = (f_B\lambda_L)/[2n(P)]$, where $f_B = f(t)$ is the (time-dependent) frequency of the Brillouin oscillations, λ_L the wavelength of the pulsed probe laser beam ($\lambda_L = 808$ nm), and $n(P)$ the refraction index of the sample material whose pressure dependence was measured earlier using optical methods. In the present study, the value of $n(P)$ of cubic H_2O ice was taken from Ref. [20] where it was determined to 120 GPa. Variations of V_L along the sample axis were traced with a resolution of 0.23–0.25 μm defined by the chosen temporal window size equal to the duration of one Brillouin oscillation. This data treatment is described in detail in the following section. Accordingly, a TDBS signal (Fig. 2) collected at one given lateral position from a 15 μm thick

sample contained up to 75 independent V_L measurements. We also used a larger temporal window of 2.5 Brillouin oscillations in order to evaluate the effect of averaging over a larger depth range on the derived $V_{L\max}$ and $V_{L\min}$. In order to further improve statistics, we performed lateral scans over distances of 20–70 μm with steps of 2–4 μm. Such combination of a high in-depth resolution and lateral scans increased the number of spatially resolved V_L data dramatically and permitted a reliable application of the envelope method: The extreme values of V_L obtained from all our TDBS signals collected at the chosen pressure could be attributed, with a high degree of confidence, to the maximal and minimal possible sound velocities in a single crystal of H_2O ice, $V_{L\max}$ and $V_{L\min}$. If we follow the majority of earlier publications claiming that the H_2O ice has cubic structure in the entire pressure range of our measurements, then our experimental dependencies $V_{L\max}(P)$ and $V_{L\min}(P)$ correspond to $V_{L\langle 111\rangle}(P)$ and $V_{L\langle 100\rangle}(P)$ in a single crystal of the cubic ice phases, respectively.

C. TDBS signal treatment

Special attention was paid to the goodness of the temporal TDBS signals collected at each lateral position on the sample (Fig. 2). In particular, frequency components of each signal were brought out by applying the fast Fourier transform (FFT) to the signal. Such treatment of the entire signal gave information about various frequencies present in the complete signal but did not give any information about the moment in time (related to the depth coordinate) when a particular frequency showed up. Thus, FFT gave information on the elastic properties along the complete path of the acoustic pulse propagation in the sample but lacks an in-depth resolution. And this is the same limitation as in the classical FDBS measurements.

In order to overcome this limitation, a demanding time-frequency analysis was applied. To simplify such analysis, each raw TDBS signal was preprocessed through a procedure in which the experimental signal $S(t)$ [Fig. 2(a)] was initially filtered to remove the nonoscillating background caused by a transient heating of the sample which modified optical reflectivity. The resulting background-free signal $s(t)$ [Fig. 2(b)] could then be described by the equation

$$s(t) = A(t)\cos[\phi(t)], \tag{1}$$

where $A(t)$ is the time-dependent amplitude of the signal and $\phi(t) = 2\pi \int f_B(t')dt' + \varphi(t)$ is the time-dependent phase of the signal. The phase could be split into a slowly varying part $2\pi \int f_B(t')dt'$, the time derivative of which is proportional to the Brillouin frequency, and a rapidly varying part $\varphi(t)$ that could exhibit abrupt jumps, for example, due to the arrival of an acoustic echo at interfaces inside the DAC. Then the background-free signal was converted to its analytical form $s_{\rm an}(t)$ by applying the Hilbert transformation which allowed separate access to the time-dependent amplitude $A(t) = \mathrm{abs}[s_{\rm an}(t)]$ and to the time-dependent phase $\phi(t) = \arg[s_{\rm an}(t)]$ [42]. The complex exponential $\exp[j\phi(t)]$ is free of variations in the amplitude [Fig. 2(c)] while information on the varying frequency is conserved. Then, any time-frequency analysis can be applied to this "damping"-free signal [Fig. 2(c)] in order to reveal the time moment when one of the frequencies emerges in the signal.

For example, the short-time Fourier transform (STFT) [43] with the window size at FWHM as small as one Brillouin cycle (if the signal quality permits) could be used. Here, the frequency corresponding to the temporal window containing the treated Brillouin cycle can be obtained. However, the temporal resolution of the STFT technique is strongly limited by the signal-to-noise ratio (SNR). For this reason, we developed a numerical equivalent of another more robust time-frequency analysis technique, namely the well-known synchronous detection technique (SDT) [44]. For this technique the preprocessing described above is mandatory. Roughly speaking, SDT is a Fourier transform without any limitation in the frequency resolution whose principal aim is to find the value f_m that maximizes the norm of the following integral $I_{\rm SD}$ in the chosen moving time window W:

$$I_{\rm SD}(t) = \int_{-\infty}^{+\infty} W(\tau - t)\exp[j\phi(\tau)]\exp(-j2\pi f_m \tau)d\tau. \tag{2}$$

Assuming a slow variation of the Brillouin frequency within the window, we can approach the term $2\pi \int f_B(t')dt'$ by the product $2\pi \tilde{f}_B t$, where $\tilde{f}_B$ is the mean Brillouin frequency within the window that one seeks to recover. If there is no abrupt phase jump, i.e., φ is constant within the window W, the value f_m found for the moving window centered on time t corresponds to $\tilde{f}_B$ indeed. We note that if φ is constant, it does not affect the norm of $I_{\rm SD}$ and corresponds to the argument of $I_{\rm SD}$ calculated with $f_m = \tilde{f}_B$. If φ is not constant within the window then both recovered values of $\tilde{f}_B$ and φ are wrong and should be ignored. The way to identify the latter situation for each position (instant of time) of the moving window is the calculation of the normalized root-mean-square error (NRMSE) serving as a goodness criterion:

$$\mathrm{NRMSE} = \frac{\mathrm{RMS}\{W(t)\exp[j\phi(t)] - W(t)\exp[j(2\pi \tilde{f}_B t + \varphi)]\}}{2}, \tag{3}$$

where the normalization by 2 relies on the maximum difference in amplitude that two trigonometric functions could have.

In the present work the signal analysis was performed recursively in order to achieve a good frequency resolution in a short calculation time: After 10 iterations we could approach the theoretical resolution of 20 kHz while the signal frequencies ranged between 25 GHz and 75 GHz. We note that the frequency resolution was not limited here by the processing technique but by the SNR. The applied signal processing method is well suited for signals containing one frequency

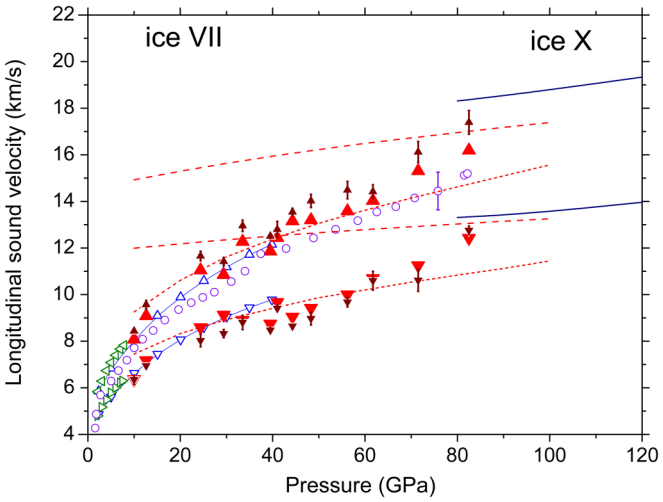

FIG. 3. Experimental and theoretical $V_L(P)$ data for H_2O ice at high pressures as reported in the present work. Symbols represent the experimental data between 10 and 82 GPa: Solid triangles pointing up and down are our experimental $V_{L\max}(P)$ and $V_{L\min}(P)$, respectively, obtained for the window sizes W equal to one (smaller dark-red triangles with error bars) and two-and-half Brillouin oscillations (larger red triangles; error bars are smaller than the symbols). Our theoretical values of $V_{L\langle 111\rangle}(P)$ and $V_{L\langle 100\rangle}(P)$ for ice VII and ice X from *ab initio* calculations are represented by dotted and dashed lines, respectively. Some of the earlier experimental and theoretical results, presented in Fig. 1 in the same style, are shown for comparison.

component varying in time. Some issues can arise for signals containing two (or more) different frequency components simultaneously. If these components are close compared with the frequency resolution, the retrieved frequency will be a weighted average of the different individual frequencies. For signals containing different but well separated frequency components, an analysis using the SDT in a limited frequency range around each individual frequency can allow an independent retrieving of the different frequency components so far. The result of such a treatment of the preprocessed signal [shown in Fig. 2(c)] is given in Fig. 2(d). Here we applied two goodness criteria: The first one requires that the SNR exceed 10 dB and the second one that the NRMSE remain below 10%. In each recorded TDBS signal we excluded from further consideration the temporal sections where at least one of the two criteria was not fulfilled. Such sections are highlighted in Fig. 2(d) with a gray background.

The frequency dependence on time [such as that shown in Fig. 2(d)] obtained for each particular lateral position could be converted to the variation of V_L in time (or depth of the acoustic pulse position at this time instant) by applying the above given classical formula. The maximal and minimal longitudinal sound velocities, $V_{L\max}$ and $V_{L\min}$, obtained after comparison of all signals collected at the chosen pressure are summarized in Fig. 3. The experimental uncertainties of these $V_{L\max}$ and $V_{L\min}$ values, and of the corresponding frequencies $f_{\max}$ and $f_{\min}$, were determined using the Cramer-Rao lower bounds expressed in Eq. (17) of Ref. [45]. We note that in this equation, the SNR is $b_0^2/(2\sigma^2)$, where b_0 is the amplitude of the signal and σ^2 is the variance of the independent Gaussian noise. In our case, the SNR is calculated by assuming that the measured signal is $S = x + n$, where x is the actual signal and n the noise. Assuming that x and n are not correlated, we finally have $\mathrm{SNR} = P_S/P_n$, where P_u stands for the power of the signal $u = \{S,x,n\}$ and the SNR is linear (not in dB). The actual value of the SNR should be $\mathrm{SNR} = P_S/P_n - 1 = (P_x + P_n)/P_n - 1 = P_x/P_n$ but the difference from the previous expression is very small and true only when the signal and the noise are indeed not correlated, which could be not the case in our measurements. The experimental uncertainty of the Brillouin frequency in our measurements, $\delta\tilde{f}_B$, has been calculated applying the formula (see Eq. (17) in Ref. [45])

$$\delta\widetilde{f}_B = \frac{1}{2\pi\,\Delta t}\sqrt{\frac{6}{N(N^2-1)\mathrm{SNR}}}, \tag{4}$$

where Δt is the time step between the neighboring points in the signal $S(t)$ and N the number of points in the window for which the Brillouin frequency $\tilde{f}_B$ was determined. Note, Eq. (4) is an implementation of the fact that the larger SNR and N, the smaller is the uncertainty $\delta\tilde{f}_B$.

D. Influence of nonhydrostatic compression

Our high-resolution TDBS measurements showed strong variations of sound velocity with the sample depth, approaching $\pm 17\%$ of $V_{L\max}(P)$ (see below). Because our polycrystalline H_2O ice samples were compressed without any pressure-transmitting medium the question could arise whether the observed V_L variations can be explained by variation of differential stresses (but not by elastic anisotropy of H_2O ice) in ice grains or groups of grains differently oriented with respect to the sound propagation direction. In the literature, the stressed state of a sample in a DAC is traditionally modeled, in the frame of continuum mechanics, as a sum of hydrostatic pressure P_0 and differential stress t_{av} acting along the sample axis coinciding with the direction of compression of the diamond anvils [46,47]. The maximal value of t_{av} is limited by the yield stress $\sigma_y(P)$ of the compressed material. In this model, the differential stress t_{av} and, accordingly, the total pressure $P = P_0 + t_{\mathrm{av}}/3$ (measured using the ruby fluorescence scale [39]) do not change along the sample axis and thus do not change V_L, density, and refractive index. However, it was shown in the recent XRD measurements combined with elastoplastic self-consistent modeling that the continuum mechanics is not suitable for the description of stressed states of individual grains in a polycrystalline sample compressed in a DAC [48]. In that work, the authors examined XRD peaks stemming from particular grains in a polycrystalline sample of cobalt having hexagonal structure at $P = 46$ GPa. The differential stress variations from grain to grain were found to be comparable with $t_{\mathrm{av}} = 1.9$ GPa but the pressure in the grains was found to be very uniform and to vary by $\leqslant 0.1\%$ of the measured value of $P = 46$ GPa. Similar pressure uniformity by moving from one grain to another was experimentally confirmed for the post-perovskite phase of $MgGeO_3$ compressed to 90 GPa [49,50]. In contrast to the hexagonal structure of cobalt, solids having cubic crystal structure (e.g., H_2O ice) exhibit a larger number of symmetry-equivalent plastic deformation mechanisms. If the strength

of each mechanism does not change, this will lead to easier differential stress relaxation and, accordingly, even smaller variations of t and P in the sample grains [49]. For this reason, the estimates we present below for the variations of t and P in the cubic ice grains of a polycrystalline sample compressed in a DAC should be considered as the upper limit. Taking the highest reported t_{av} value for H_2O ice, reaching $\sim$10% of the measured pressure value [24], we obtained $t_{av} \approx 8$ GPa at $P = 80$ GPa and estimated pressure variations in the ice grains along the sample axis to be $\leqslant$0.3 GPa. Such pressure variations would result in V_L variations along the sample axis of $<$0.2% which are negligible when compared with other experimental uncertainties and with the total V_L variations approaching 34%, as revealed in our TDBS measurements. Furthermore, it was experimentally and theoretically verified in our earlier work that the effect of optical anisotropy in the ice grains and in the diamond anvils induced along the sample depth by differential stresses is very weak, equivalent to less than 2% of a potential variation of the measured Brillouin frequency (or V_L) [35]. Given these considerations and the fact that elastic moduli and density of any solid depend on pressure only (not on the deviatoric stress, equivalent to the shear stress; e.g., [48,51]) the V_L variations along the sample depth recognized in our TDBS measurements were caused by the elastic anisotropy of H_2O ice exclusively.

For completeness, we also estimated influence of the lateral (radial) pressure gradients in our ice samples on the measured V_L applying results of the continuum mechanics modeling of the plastic deformation of a solid disk compressed between diamond anvils (see Chap. 1.3 in [47]). Using our sample sizes and the highest reported t_{av} for H_2O ice in the equation for "nonflowing area," we obtained pressure variations throughout the entire optoacoustic generators of $<$3%, for the smaller generator at 82 GPa, and $<$7%, for the larger generator at 57 GPa. Then, applying the measured pressure dependence of V_L (Fig. 1 or Fig. 3), we obtained the lateral V_L variations of $<$1.5%, for the smaller generator, and $<$2.5%, for the larger one. Again, these values are significantly smaller than the sound velocity variations in our TDBS measurements approaching the total amplitude of 34%. In summary, neither lateral pressure gradients nor variation of differential stresses in the grains along the sample depth could cause the Brillouin frequency variations revealed in the present work. They can be explained by a large elastic anisotropy of H_2O ice only.

E. *Ab initio* calculations

Calculations of elastic properties at high pressures from first principles require knowledge of the crystal structure of the examined material as an input. In this work, the calculations were guided by the most accepted model of the H_2O ice structure at room temperature and pressures above $\sim$2.5 GPa where oxygen anions form a body-centered cubic sublattice and protons are located between the neighboring O anions; see, e.g., [22].

Our calculations of elastic properties of the cubic phases of H_2O ice were performed using the first-principles plane-wave pseudopotential method based on the density functional theory (DFT) implemented in the Vienna *ab initio* simulation package (VASP) [52–54]. The generalized gradient approximation (GGA) parametrized by Perdew, Burke, and Ernzerhof (PBE) was adopted to describe the electronic exchange-correlation potential [55]. The projector augmented wave (PAW) method [56,57] was employed to model interactions between nuclei and electrons. The electron wave functions were expanded in plane waves with cutoff energy of 870 eV. In the case of cubic ice X we chose a k mesh of $8 \times 8 \times 8$ to sample the irreducible cubic Brillouin zone whereas for cubic ice VII represented by a $2 \times 2 \times 2$ supercell, we used a k mesh of $4 \times 4 \times 4$. The unit cell geometry including volume, shape, and atomic positions was fully relaxed until the target external pressure, approximated by the Pulay stress, was achieved. In fact, the Pulay stress is the trace of the calculated external stress tensor. The total energy tolerance for the electronic minimization was set as 1×10^{-6} eV and the interatomic force tolerance for the geometric optimization was set as 0.01 eV/Å.

By simulation of the ice VII structure, the proton-disordered configurations at around zero pressure were obtained using the following procedure: An ordered supercell containing $2 \times 2 \times 2$ unit cells of ice X was set up with the volume close to that of ice VII. Standard *ab initio* molecular dynamics (MD) calculations [53] were performed then at 300 K with fixed oxygen positions while the protons were able to move. A Verlet algorithm [58] was used to integrate Newton's equations of motion with a time step of 1.5 fs. This procedure resulted in a cubic supercell with quasirandom H_2O molecule orientations. Taking the generated supercell, its geometry including volume, shape, and positions of protons and oxygen anions was fully relaxed for different pressures from 10 to 100 GPa with an interval of 10 GPa by using the static DFT calculations described above. Identical electronic structure parameters were employed for the static DFT and *ab initio* MD calculations.

For each pressure, single-crystal elastic moduli of the cubic ice phases were calculated. The elastic tensor was determined by performing six finite distortions of the lattice and deriving the elastic constants from the strain-stress relation as implemented in VASP internally.

III. RESULTS

A. Distribution of V_L in ice VII and the phase transition to ice X

In order to further substantiate the contradictions discussed in the Introduction, we first elucidated the observed in the earlier FDBS studies convergence of $V_{L\,av}(P)$ to $V_{L\,max}(P)$. We have found that this convergence is a result of elastic anisotropy of ice VII causing a strongly asymmetric shape of the Brillouin peak collected from a polycrystalline texture-free sample: In order to model the Brillouin peak shape we calculated the distribution of V_L in a single crystal of ice VII. Using $C_{ij}(P)$ of ice VII from FDBS at 40 GPa [30], we calculated V_L for 20 000 discrete uniformly spread directions in a single crystal and counted the number of directions with the same V_L. The resulting velocity histogram with the bin size of 10 m/s is shown in the inset of Fig. 1. The asymmetric distribution of V_L in the histogram implies that a FDBS peak collected from a texture-free polycrystalline ice VII sample at 40 GPa should be similarly asymmetric. Both the distribution maximum and its center of mass are strongly shifted to the

upper limit value $V_{L\langle 111\rangle}$. In the case of a weak signal from a microscopic cubic ice sample in a DAC, the low-velocity flank of the FDBS peak could become indistinguishable from background. Similar analyses of the V_L distribution for ice X using $C_{ij}(P)$, predicted theoretically by Journaux *et al.* [3] and in this work (see below), led to the same results: The dependence $V_{L\mathrm{av}}(P)$ in classical FDBS measurements on *polycrystalline texture-free* samples of ice X should approach the dependence $V_{L\max}(P) = V_{L\langle 111\rangle}(P)$, provided the phase exists.

Further, we performed first-principles calculations of $C_{ij}(P)$ for ice X at pressures between 10 and 100 GPa (see below for a detailed description of the results) in order to verify our linear extrapolation of the previous theoretical data, obtained between 80 and 450 GPa [3], to pressures below 80 GPa. Our calculations confirmed that ice X is highly rigid and both $C_{ij}(P)$ and sound velocities only weakly change with pressure (Fig. 1). These findings, combined with the above discussed tendency of $V_{L\mathrm{av}}(P)$ to approach $V_{L\max}(P)$, suggest that the ice X did not appear in the earlier FDBS experiments to 80 GPa [26,29], provided the polycrystalline samples of H_2O ice remained texture-free. This is because the formation of ice X between 40 and 80 GPa would cause a jump of $V_{L\mathrm{av}}(P)$ to significantly higher values instead of a continuous increase reported in these classical FDBS measurements. Such a jump should occur in texture-free cubic H_2O ice samples compressed in a DAC because (i) the transition from ice VII to ice X must be hysteresisless, (ii) pressure variations along the sample depth are negligibly small, (iii) $V_{L\mathrm{av}}(P)$ of texture-free cubic ice VII and ice X samples approaches $V_{L\max}(P)$, and (iv) up to 80 GPa the theoretical $V_{L\max}(P)$ of ice X is much higher than the reported experimental $V_{L\mathrm{av}}(P)$, corresponding to $V_{L\max}(P)$ of ice VII (Fig. 1). Obviously, the above considerations and conclusions are obsolete if the earlier classical FDBS measurements were performed using unfocused laser beams and/or the spectra were not collected from one and the same sample region after each pressure increase. Texture could not obscure the transition in these experiments because no systematic difference in $V_{L\mathrm{av}}$ was recognized by the application of the backscattering and forward-scattering geometries [29].

B. Sound velocities of H_2O ice

At each chosen pressure, starting from 82 GPa or 57 GPa, we collected up to 40 TDBS signals (see Fig. 2 for an example) by lateral scanning over the samples of H_2O ice. Results of the data analysis (described above in Sec. II C) are summarized in Fig. 3 where our experimental values of $V_{L\max}(P)$ and $V_{L\min}(P)$ between 10 GPa and 82 GPa, obtained for two temporal windows of 1 and 2.5 Brillouin oscillations, are shown. At first glance, our experimental data appear to scatter significantly (Fig. 3). However, the scattering is smaller or much smaller (depending on pressure) than the width of the Brillouin peaks reported in the earlier classical FDBS measurements [29], the only FDBS study of H_2O ice in a DAC which presents experimental spectra. In other published reports of classical FDBS measurements only results of the spectra treatments were presented. This could explain, at least partially, a much smoother change of the Brillouin frequencies with pressure in these publications when compared with our experimental data points (Fig. 3).

Experimental uncertainties for our $V_{L\max}(P)$ and $V_{L\min}(P)$ values, for both temporal windows, were determined using Eq. (4) and only those for the narrower temporal window were larger than the symbols in Fig. 3. We note that by calculation of uncertainties of V_L from the TDBS signals, we did not consider uncertainties in the experimental values of $n(P)$, reported to be small [20]. The smaller uncertainties in $V_{L\max}(P)$ and $V_{L\min}(P)$ as well as a smaller deviation of $V_{L\max}(P)$ from $V_{L\min}(P)$ found for the wider temporal window are, obviously, due to the fact that the TDBS signals were averaged over larger depth distances and therefore over a larger number of grains. Nevertheless, the difference between $V_{L\max}(P)$ and $V_{L\min}(P)$ for the wider window is similar to that observed in the classical FDBS measurements on polycrystalline H_2O ice samples where the envelope method was applied [30]. For the narrower temporal window, we obtained $V_{L\max}(P)$ and $V_{L\min}(P)$ (Fig. 3) following the same tendency as velocities in the single-crystal ice VII measured to 8 GPa [28]. As already elucidated above, the earlier reported dependencies $V_{L\mathrm{av}}(P)$ approach our $V_{L\max}(P)$. All these observations legitimated our use of $V_{L\max}(P)$ and $V_{L\min}(P)$ for the narrower temporal window to determine $C_{ij}(P)$ of H_2O ice at pressures above 10 GPa.

In what follows we assumed, after the most accepted model, that H_2O ice has remained cubic over the entire pressure range of our measurements. In this case, we could set $V_{L\max}(P) = V_{L\langle 111\rangle}(P)$ and $V_{L\min}(P) = V_{L\langle 100\rangle}(P)$, the fastest and the slowest sound propagation directions in a cubic crystal. In order to obtain $C_{ij}(P)$ we needed $B(P)$ as an input parameter from an independently determined equation of state, $\rho(P)$. Unfortunately, the earlier published $\rho(P)$ [17,19,23,24,26] scatter strongly and there was no convincing criterion to prefer one over the other. For this reason, we applied a recursive procedure to select the most reliable one: For each reported pair of $\rho(P)$ and $B(P) = [C_{11}(P) + 2C_{12}(P)]/3$ we derived the moduli $C_{ij}(P)$ using our experimental $V_{L\langle 111\rangle}(P)$ and $V_{L\langle 100\rangle}(P)$. Then, these $C_{ij}(P)$ were tested with respect to the mechanical stability criterion requiring $(C_{11} - C_{12}) > 0$ [59,60]. Surprisingly, only one experimental $\rho(P)$ published in Ref. [23] led to $C_{ij}(P)$ satisfying this criterion over the entire pressure range and, accordingly, was adopted. It should be mentioned that this equation of state also gave the best agreement with our and with the earlier first-principles calculations [17]. Our experimental moduli $C_{ij}(P)$ and $G(P)$ of the cubic H_2O ice are shown in Fig. 4. For error propagation, only the uncertainties of our TDBS data were taken into account. Subsequently, pressure dependencies of the maximal and minimal transversal sound velocities, $V_{T\max}(P) = V_{T\langle 100\rangle}(P)$ and $V_{T\min}(P) = V_{T\langle 110\rangle}(P)$, were calculated (Fig. 5). Our $V_{T\langle 100\rangle}(P)$ and $V_{T\langle 110\rangle}(P)$ agree reasonably well with those reported in the earlier single-crystal measurements to 8 GPa [28] and embrace $V_{T\max}(P)$ and $V_{T\min}(P)$, found in the FDBS measurements on polycrystalline samples applying the envelope method [30], as well as $V_{T\mathrm{av}}(P)$ from Ref. [29]. Last but not least, a discontinuity in our $V_{T\langle 110\rangle}(P)$ dependence was observed around 40 GPa and its possible nature is discussed below. In summary, our experimental TDBS data provide reasonable explanations for all earlier reported inconsistent

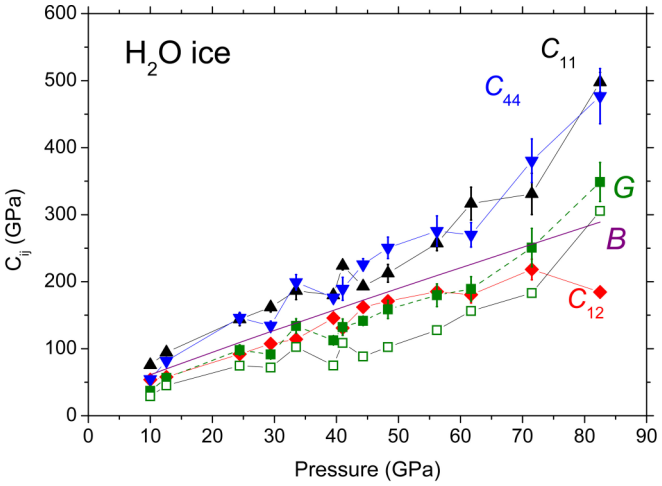

FIG. 4. Pressure dependencies of the single-crystal elastic moduli $C_{ij}(P)$ of H_2O ice derived under the assumption that the ice structure is cubic in the entire pressure range. Only experimental TDBS data, obtained for the narrower window (Fig. 3), were used to determine the shown $C_{ij}(P)$. Solid line represents $B(P)$ reported in Ref. [23]. Solid triangles pointing up and down show $C_{11}(P)$ and $C_{44}(P)$, respectively. Solid rhombuses and squares show our $C_{12}(P)$ and $G(P)$, respectively, where the latter was calculated from $C_{ij}(P)$ using the Voigt approximation, $G(P) = [C_{11}(P) - C_{12}(P) + 3C_{44}(P)]/5$. Open squares show $G(P)$ calculated using the Voigt-Reuss-Hill approximation (the experimental uncertainties, not shown for clarity, are the same as for the Voigt approximation).

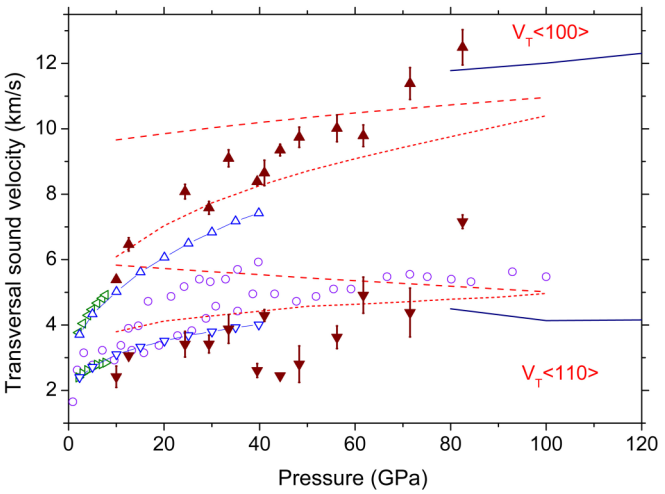

FIG. 5. Experimental and theoretical $V_T(P)$ values for cubic H_2O ice. Symbols represent experimental data: Solid dark-red triangles pointing up and down show, respectively, our $V_{T\langle 100\rangle}(P)$ and $V_{T\langle 110\rangle}(P)$ between 10 and 82 GPa derived using the experimental $C_{ij}(P)$ depicted in Fig. 4. Open green triangles pointing left and right show $V_{T\langle 100\rangle}(P)$ and $V_{T\langle 110\rangle}(P)$, respectively, measured for single crystals of ice VII by Shimizu *et al.* [28]; open triangles pointing up and down represent the same values calculated from $C_{ij}(P)$ reported by Zha *et al.* [30]; circles are $V_{T\,\mathrm{av}}(P)$ measured for polycrystalline ice samples by Ahart *et al.* [29]. Lines represent theoretical values of $V_{T\langle 100\rangle}(P)$ and $V_{T\langle 110\rangle}(P)$: Dotted lines, our calculations for ice VII; dashed lines, our calculations for ice X; solid lines, earlier results of Journaux *et al.* for ice X [3].

FDBS data on sound velocities and elastic moduli of the cubic H_2O ice obtained for single crystals and for polycrystalline samples.

C. Results of the first-principles calculations

The above presented experimental findings were supported by the first-principles calculations of $C_{ij}(P)$ and $\rho(P)$ for ice VII and ice X (Fig. 6) from which sound velocities of the longitudinal and transversal waves propagating in different directions in single crystals can be deduced. For the both phases, we calculated first $\rho(P)$ [Fig. 6(a)] and $C_{ij}(P)$ [Figs. 6(b) and 6(c)] and then $V_{L\langle 111\rangle}(P)$ and $V_{L\langle 100\rangle}(P)$ (Fig. 3) as well as $V_{T\langle 100\rangle}(P)$ and $V_{T\langle 110\rangle}(P)$ (Fig. 5). As already mentioned, our theoretical equation of state, $\rho(P)$, and $B(P)$ were found to fit best the corresponding experimental curves reported in Ref. [23]. General tendencies in the pressure dependencies of our experimental $C_{ij}(P)$ and $G(P)$, with the exception of the data point at the highest pressure, are reasonably well reproduced by our calculations. Namely, the theoretical $C_{11}(P)$ and $C_{44}(P)$ do not differ strongly from the corresponding experimental values, typically by $<15\%$, but deviate more from each other than the experimental ones. The calculated dependencies $C_{12}(P)$ and $G(P)$ agree well with the experimental data in most of the pressure range. The similarly high values of these moduli are well reproduced, except the last experimental data point at 82 GPa. Sources of moderate discrepancies between the theoretical and experimental data can be of different natures: First, even for simple crystal structures of binary compounds (e.g., NaCl type) with known fixed positions of both cations and anions, deviation of experimental bulk moduli from those calculated using the GGA approximation can reach 15% [61]. The crystal structure of H_2O, especially of ice VII, is much more complicated than that of a simple NaCl type structure and is less well verified at pressures above $\sim$50 GPa because the proton positions appear to change upon compression. Second, temperature effects were not taken into account in our *ab initio* calculations performed at $T = 0$ K. Third, our model does not consider possible displacement of protons to octahedral interstitials of the O sublattice proposed in Ref. [22]. Displacement of protons within the lattice of H_2O ice can strongly influence its elastic moduli, as impressively demonstrated by our calculations: A relatively small shift of protons from an asymmetric position between the O atoms in ice VII to a symmetric one in ice X causes a dramatic moduli increase [Figs. 6(b) and 6(c)]. Similarly, we did not consider a possibly significant deviation of the ice structure from cubic symmetry as proposed in the recent XRD studies [21]. Accordingly, a moderate disagreement of the calculated and measured $C_{ij}(P)$ could be a manifestation of subtle changes in the ice crystal structure upon compression. Finally, we would like to remind the reader that a reliable transferable analytic functional describing the O-H interaction in H_2O ice is still not established [17]. This limits significantly all *ab initio* calculations on H_2O ice properties, including ours: It impedes the demanding modeling of the local structure of ice VII having orientationally and, maybe, positionally disordered H_2O molecules or protons alone. In addition to elastic moduli of ice VII, we found in our calculations that

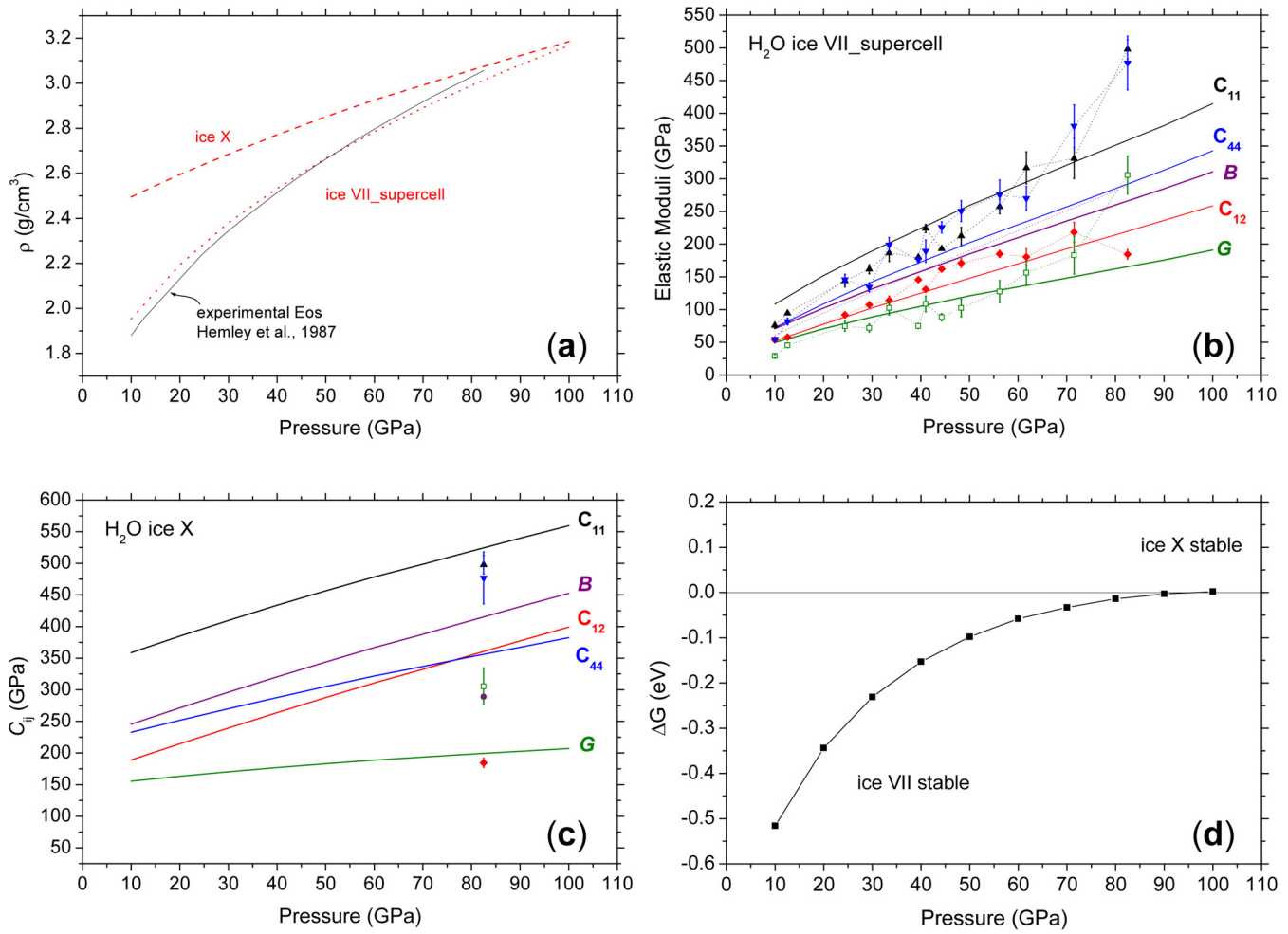

FIG. 6. Results of present *ab initio* calculations for the cubic ice phases VII and X between 10 and 100 GPa. (a) Calculated densities of ice VII and ice X are represented by the dotted and dashed red line, respectively, and compared with the experimental EOS (solid line) reported in Ref. [23] which we used to derive $C_{ij}(P)$ values from the measured $V_{L\max}(P)$ and $V_{L\min}(P)$. (b) Elastic moduli of ice VII calculated for the $2 \times 2 \times 2$ supercell model are represented by thick solid lines. The theoretical $G(P)$ is derived from the $C_{ij}(P)$ using the Voigt-Reuss-Hill approximation. The calculated values are compared with our experimental results shown in Fig. 4 (symbols connected by thin solid lines). (c) Calculated elastic moduli of ice X represented by thick solid lines. The theoretical $G(P)$ is derived from the shown $C_{ij}(P)$ using the Voigt-Reuss-Hill approximation. The experimental data points at 82 GPa (see Fig. 4) are shown for comparison. (d) Calculated Gibbs free energy difference between ice VII and ice X at $T = 0$ K, shown by connected solid squares.

between 10 GPa and 100 GPa the supercell of this phase has a local minimum on the total energy scale and that the H_2O units are recognizable. However, the number of protons located symmetrically between the adjacent O atoms grows upon compression. We expect that the present experimental results can be used in future theoretical studies aiming at the improvement or optimization of the basic interaction potential between H and O. Such optimization and development of a more realistic structural model of ice VII, including positions of protons, should be a subject of a separate work. We consider our present calculations as a first step to the solution of this demanding problem. Despite the shortages in our calculations of $C_{ij}(P)$ of cubic H_2O ice, our theoretical limits for $V_L(P)$ of ice VII agree reasonably well with those we obtained from the TDBS measurements. There are minor differences in the slopes of our calculated and experimental $V_{L\langle 111\rangle}(P)$ and $V_{L\langle 100\rangle}(P)$ which can probably be explained by the above listed limitations of our theoretical approach. Finally, we calculated the Gibbs free energies of ice VII and ice X at $T = 0$ K. Their comparison [Fig. 6(d)] suggests that the ice VII remains stable up to 90 GPa provided the temperature increase to 293 K does not shift the phase equilibrium pressure significantly. Another confirmation of this finding could be a significant discrepancy between the elastic moduli we have derived from the TDBS measurements and those predicted theoretically for ice X [Fig. 6(c)]. However, at 82 GPa our experimental $C_{ij}(P)$ do not agree well with the theoretical values for the ice VII either and a transition to a phase other than ice X could be the cause.

IV. DISCUSSION

Comparison of our experimental longitudinal sound velocities with the theoretical $V_{L\langle 111\rangle}(P)$ and $V_{L\langle 100\rangle}(P)$ for the two cubic H_2O ice phases (see Fig. 3) suggests that ice X does not occur at $P \leqslant 60$ GPa, not even as a minor coexisting phase. Our TDBS technique has sufficiently high spatial resolution to

reveal any regions within the samples where $V_{L\max}$ approaches the theoretical $V_{L\langle 111\rangle}$ of the ice X. At higher pressures our $V_L(P)$ data (Fig. 3) do not permit unambiguous conclusion about the existence of the ice X phase. However, the persistence of ice VII to the highest pressure of 82 GPa follows from the comparison of our experimental and theoretical $V_T(P)$ for both phases (Fig. 5): Our theoretical $V_{T\min}(P) = V_{T\langle 110\rangle}(P)$ of ice X, agreeing well with the earlier predictions [3], decreases with pressure but the experimental one increases. It should be mentioned here that a significant scattering of our experimental $V_T(P)$ values can be explained by accumulation of the measurement uncertainties of $V_{L\max}(P)$, $V_{L\min}(P)$, and $B(P)$ needed to derive $V_{T\langle 100\rangle}(P)$ and $V_{T\langle 110\rangle}(P)$. Our *ab initio* calculations [Fig. 6(d)] of the phase equilibrium also exclude the transition from ice VII into ice X at $P < 90$ GPa, similarly to an earlier prediction [16]. Finally, a discontinuity in the experimental dependencies $V_{L\min}(P)$ and $V_{T\langle 110\rangle}(P)$ at about 40 GPa (Fig. 3 and Fig. 5) could be an indication of a subtle change of the ice VII elasticity possibly related to a structural change proposed in the recent XRD studies and/or to the kink in $n(P)$ at the same pressure (see Introduction). Another indication of a phase transition could be an elevated elastic anisotropy factor A between 8 and 14 we obtained from the experimental $C_{ij}(P)$ values between 40 and 55 GPa while at $P < 40$ GPa and $P > 60$ GPa the elastic anisotropy factor was below 6.

Our experimental dependence of the shear modulus of cubic H_2O ice on pressure, $G(P)$, (Fig. 4) implies a significant increase of the ice hardness to values typical for hard ceramics if a nearly linear correlation of these material properties established in the literature [62] is adopted: At $P = 24$ GPa we obtained for cubic H_2O ice $G \approx 86$ GPa, similar to that of TiC at ambient conditions, while at $P = 82$ GPa we measured $G \approx 330$ GPa, not far from that of cubic BN, the second hardest material after diamond at atmospheric pressure. Furthermore, from our TDBS results it follows that at $P > 10$ GPa the ratio B/G is close to unity, if the Voigt approximation is used to calculate the shear modulus from $C_{ij}(P)$. This suggests, according to the Pugh criterion [63], a high brittleness of cubic H_2O ice. Another indication of brittleness of cubic H_2O ice is a large and growing negative value of Cauchy pressure defined as $(C_{12} - C_{44})$ [64]. Such properties combination, typical rather for ceramics, should strongly influence internal structure and seismic activity of the H_2O ice rich planets, especially those having weak or no intrinsic heat sources, e.g., Uranus [5].

The high hardness combined with a significant elastic anisotropy, revealed in this work, could explain the considerable systematic deviations of the interplanar distances for different crystallographic orientations $d(hkl)$ observed in the earlier XRD studies on the cubic ice phases compressed in a DAC [21,24]. In contrast to sound velocities, $d(hkl)$ of ice grains are strongly influenced by differential stresses, their distribution and orientation in the sample volume. This is valid for any solid compressed nonhydrostatically in a DAC and limits accuracy of bulk modulus measurements using the XRD technique. Because H_2O ice does not permit the use of any pressure medium, the recognized strong scattering of the experimental dependencies $\rho(P)$ and $B(P)$ cannot be avoided in the high-pressure XRD measurements.

Our modeling of the peak shape in classical FDBS spectra of *texture-free polycrystalline* samples of *elastically anisotropic* solids (cubic H_2O ice in this work) demonstrated a limited usability of FDBS by determining average sound velocities: In the case of cubic H_2O ice neither the maximum of the Brillouin peak (whose ideal shape was reproduced by the calculated V_L distribution in a single crystal) nor the most probable sound velocity (center of mass of the distribution) agreed with the sound velocity derived applying the isotropic elastic moduli B and G calculated using the same C_{ij} moduli via the Voigt or Voigt-Reuss-Hill approximation (see caption of Fig. 1). Moreover, the deviation is systematic and can vary if the elastic anisotropy changes upon compression or heating. Ignoring of this fact can lead to incorrect values of average sound velocities in elastically anisotropic polycrystalline solids or erroneous results and conclusions about phase transitions as could be the case for cubic H_2O ice. Apparently, such uncertainties are not expected in the FDBS studies on sufficiently large single crystals, both at atmospheric and at high pressures, but the vast majority of such type of studies was already completed in the past. The classical FDBS has also been successfully applied for many decades to measure elastic properties (also at high pressures and high temperatures) of numerous isotropic systems such as organic samples, liquids, polymers, nanostructured thin films, and glassy materials. However, nowadays an increasing number of novel materials are available only as polycrystalline bodies or coatings providing inherent limitations to the use of the traditional FDBS. This is a motivation to develop new techniques providing deeper insights into elastic behavior of such samples with μm or sub-μm spatial resolution.

We have demonstrated in this work that the TDBS technique is quite suitable for the measurement of sound velocities and elastic anisotropy, as well as for revealing local inhomogeneities in any transparent solid, both at atmospheric and at high pressures. Knowledge of the refractive index is needed in order to derive the sound velocities from the Brillouin frequencies obtained using the TDBS technique. Knowledge of the density and/or EOS is needed in the next step, to derive single-crystal elastic moduli $C_{ij}(P)$. These requirements are common to both FDBS and TDBS, though. One of the advantages of the TDBS technique is the ability to reveal elastic anisotropy of examined polycrystalline solids which can be obscured in classical FDBS measurements. This capability permits us to avoid hasty conclusions about the elastic properties or phase transitions in an anisotropic sample upon change of pressure or temperature.

In contrast to the classical FDBS, the high spatial resolution of the TDBS, especially its high axial resolution, excludes data compromising when differential stresses become significant in compressed or deformed single crystals. The main cause of the data compromising by use of the FDBS is the elastic anisotropy: Nonhydrostatic compression/deformation causes recrystallization, formation of domains, and cracking of initially single crystal samples. The resulting smaller grains differently oriented with respect to each other and to the initial single crystal cause degradation of the classical FDBS spectra manifesting itself in splitting and broadening of the Brillouin peaks. The TDBS technique permits, in contrast, detection and imaging of such sample states due to its capability of 3D mapping of the sound velocity distribution with a high spatial resolution [41]. Previously, degradation of single

crystals upon nonhydrostatic compression in a DAC and their transformation in polycrystals has been reported in the literature, especially in the XRD studies. However, none of the earlier techniques provided the sufficiently high axial resolution permitting the *in-situ* examination of such states and their evolution upon compression.

The capabilities of TDBS promise a significant extension of our knowledge about the state of strongly densified matter. Its high spatial resolution permits quantitative measurements of sound velocities, elastic anisotropy, and local inhomogeneities in any transparent solid compressed to pressures in excess of 100 GPa where the classical FDBS encounters its limits due to small sample volumes and lateral pressure gradients [31,33]. Because the lateral resolution of the optical methods (up to $\sim 1\,\mu$m) used to measure the refractive index upon compression [20,38] is similar to that of the TDBS technique, determination of sound velocities on severe compression should be straightforward. Combined with the synchrotron-based XRD, the TDBS technique could help in establishing the primary pressure scale at pressures exceeding 100 GPa whose absence is considered a central problem in solid state physics [65]. Presently, equations of state of some metals (e.g., Au, Pt, or Re) derived from shock wave compression are used for pressure measurement or for the development of secondary pressure scales such as shift of the $R1$ fluorescence line of ruby or of the high-frequency edge of the diamond Raman band [33,39,66]. Reliability of these equations of state, especially systematic deviations, are difficult to evaluate due to the application of unsupported (or basic) theoretical models of the P-T behavior of solids by reduction of the high pressure–high temperature shock compression data to the room temperature–static pressure conditions [65]. Application of the TDBS technique (similarly to the FDBS technique) makes unnecessary the preliminary knowledge of the density of the examined crystalline samples throughout the whole pressure range of intended experiments. Starting from the pressure where this value is known, a combination of the TDBS and XRD measurements permits the extension of the EOS under strong compression in a DAC applying the basic expression $\delta P = B(P)\,\delta\rho(P)/\rho(P)$. Here, $\delta\rho(P)$ and $\rho(P)$ can be determined from the XRD data, provided the sample is crystalline and the pressure increment is small. In order to derive $B(P)$ from the TDBS measurements, the elastic anisotropy A should be examined at the starting pressure using the statistical approach described above. Then, the constancy of A should be confirmed upon the pressure increase, and the values $V_{L\max}$ and $V_{L\min}$ determined by performing the 3D mapping of the V_L distribution. In the final step, the expressions describing elastic anisotropy A, density increment, and $V_{L\max}$ and $V_{L\min}$ permit calculation of the bulk modulus $B(P)$. Summarizing, the TDBS technique combined with the synchrotron-based XRD technique provides the best opportunity to establish the primary pressure scale at pressures exceeding 100 GPa.

V. CONCLUSION

In this work we have extended studies on sound velocities and single-crystal elastic moduli of compressed H_2O ice to pressures of 82GPa. The pressure region where $V_{L\langle 111\rangle}(P)$ and $V_{L\langle 100\rangle}(P)$ in a single crystal of cubic H_2O ice are measured was doubled. The sound velocities were extracted from the Brillouin frequency distributions in polycrystalline H_2O ice samples compressed in a DAC. For this purpose, we applied the TDBS technique having a sub-μm in-depth resolution. This technique provided $V_{L\max}(P)$ and $V_{L\min}(P)$ much closer to $V_{L\langle 111\rangle}(P)$ and $V_{L\langle 100\rangle}(P)$, respectively, than in the earlier classical FDBS experiments. Obtained sound velocities allowed evaluation of reliability of the existing equations of state of cubic H_2O ice measured using x-ray diffraction. Only one of the earlier reported EOSs [23] was found to satisfy the mechanical stability criterion $(C_{11}-C_{12}) > 0$ in the entire pressure range. However, this statement as well as some other deductions are valid only if the crystal structure of H_2O ice remained cubic in our measurements. Applying this EOS, we derived $C_{ij}(P)$ and $G(P)$ and estimated the transversal sound velocities $V_{T\langle 100\rangle}(P)$ and $V_{T\langle 110\rangle}(P)$ for cubic H_2O ice to 82 GPa. Our data indicated a significant elastic anisotropy and a high hardness of the cubic H_2O ice which could explain the discrepancies in the earlier reported EOS and FDBS data. Our experimental results were supported by *ab initio* calculations of elastic moduli of ice VII and ice X between 10 GPa and 100 GPa. Taken together, our experimental and theoretical results imply that ice X does not form at pressures below 80 GPa. A high spatial resolution of the TDBS technique demonstrates its suitability for the measurement of the elastic properties of transparent solids at pressures in excess of 100 GPa and for establishment of the primary pressure scale if combined with high-resolution synchrotron-based x-ray diffraction.

ACKNOWLEDGMENTS

We are grateful to D. Gasteau, B. Castagnede, Y. Roussigne, and S. Merkel for fruitful discussions, as well as to J. E. Lowther, B. Joseph, and O. Tschauner for detailed comments. The work was financially supported by the ANR BLANC 2011 program (France) in the framework of the project "LUDACism." Q.M.H. acknowledges financial support from the MoST of China under Grant No. 2016CB644001 and from NSFC under Grant No. 51271181.

[1] W. B. Hubbard, W. J. Nellis, A. C. Mitchell, N. C. Holmes, S. S. Limaye, and P. C. McCandless, Science **253**, 648 (1991).

[2] A. N. Dunaeva, D. V. Antsyshkin, and O. L. Kuskov, Sol. Syst. Res. **44**, 202 (2010).

[3] B. Journaux, R. Caracas, P. Carrez, K. Gouriet, P. Cordier, and I. Daniel, Phys. Earth Planet. Inter. **236**, 10 (2014).

[4] W. B. Hubbard, *Planetary Interiors* (Van Nostrand Reinhold Company, New York, 1984).

[5] M. Podolak and R. Helled, Astrophys. J. Lett. **759**, L32 (2012).

[6] R. Fu, R. J. O'Connell, and D. D. Sasselov, Astrophys. J. **708**, 1326 (2010).

[7] A. Leger, F. Selsis, C. Sotin, T. Guillot, D. Despois, D. Mawet, M. Ollivier, A. Labeque, C. Valette, F. Brachet, B. Chazelas, and H. Lammer, Icarus **169**, 499 (2004).
[8] W. B. Holzapfel, J. Chem. Phys. **56**, 712 (1972).
[9] R. J. Hemley, Annu. Rev. Phys. Chem. **51**, 763 (2000).
[10] A. F. Goncharov and R. J. Hemley, Chem. Soc. Rev. **35**, 899 (2006).
[11] W. F. Kuhs, J. L. Finney, C. Vettier, and D. V. Bliss, J. Chem. Phys. **81**, 3612 (1984).
[12] R. J. Nelmes, J. S. Loveday, W. G. Marshall, G. Hamel, J. M. Besson, and S. Klotz, Phys. Rev. Lett. **81**, 2719 (1998).
[13] P. Pruzan, J. C. Chervin, and B. Canny, J. Chem. Phys. **99**, 9842 (1993).
[14] J. D. Jorgensen, R. A. Beyerlein, N. Watanabe, and T. G. Worlton, J. Chem. Phys. **81**, 3211 (1984).
[15] K. R. Hirsch and W. B. Holzapfel, Phys. Lett. A **101**, 142 (1984).
[16] M. Benoit, A. H. Romero, and D. Marx, Phys. Rev. Lett. **89**, 145501 (2002).
[17] M. French and R. Redmer, Phys. Rev. B **91**, 014308 (2015).
[18] M. Benoit, D. Marx, and M. Parrinello, Nature (London) **392**, 258 (1998).
[19] P. Loubeyre, R. LeToullec, E. Wolanin, M. Hanfand, and D. Hausermann, Nature (London) **397**, 503 (1999).
[20] C.-S. Zha, R. J. Hemley, S. A. Gramsch, H.-K. Mao, and W. A. Bassett, J. Chem. Phys. **126**, 074506 (2007).
[21] M. Somayazulu, J. F. Shu, C. S. Zha, A. F. Goncharov, O. Tschauner, H. K. Mao, and R. J. Hemley, J. Chem. Phys. **128**, 064510 (2008).
[22] M. Guthrie, R. Boehler, C. A. Tulk, J. J. Molaison, A. M. dos Santos, K. Li, and R. J. Hemley, Proc. Natl. Acad. Sci. USA **110**, 10552 (2013).
[23] R. J. Hemley, A. P. Jephcoat, H. K. Mao, C. S. Zha, L. W. Finger, and D. E. Cox, Nature (London) **330**, 737 (1987).
[24] E. Wolanin, P. Pruzan, J. C. Chervin, B. Canny, M. Gauthier, D. Hausermann, and M. Hanfland, Phys. Rev. B **56**, 5781 (1997).
[25] E. Sugimura, T. Iitaka, K. Hirose, K. Kawamura, N. Sata, and Y. Ohishi, Phys. Rev. B **77**, 214103 (2008).
[26] A. Polian and M. Grimsditch, Phys. Rev. Lett. **52**, 1312 (1984).
[27] J. M. Besson, M. Kobayashi, T. Nakai, S. Endo, and P. Pruzan, Phys. Rev. B **55**, 11191 (1997).
[28] H. Shimizu, M. Ohnishi, S. Sasaki, and Y. Ishibashi, Phys. Rev. Lett. **74**, 2820 (1995).
[29] M. Ahart, M. Somayazulu, S. A. Gramsch, R. Boehler, H.-K. Mao, and R. J. Hemley, J. Chem. Phys. **134**, 124517 (2011).
[30] C.-S. Zha, H.-K. Mao, R. J. Hemley, and T. S. Duffy, Rev. High Pressure Sci. Technol. **7**, 739 (1998).
[31] D. M. Trots, A. Kurnosov, T. B. Ballaran, S. Tkachev, K. Zhuravlev, V. Prakapenka, M. Berkowski, and D. J. Frost, J. Geophys. Res.: Solid Earth **118**, 5805 (2013).
[32] C. S. Zha, H. K. Mao, and R. J. Hemley, Proc. Natl. Acad. Sci. USA **97**, 13494 (2000).
[33] K. K. Zhuravlev, A. F. Goncharov, S. N. Tkachev, P. Dera, and V. B. Prakapenka, J. Appl. Phys. **113**, 113503 (2013).
[34] N. Dubrovinskaia, L. Dubrovinsky, N. A. Solopova, A. Abakumov, S. Turner, M. Hanfland, E. Bykova, M. Bykov, C. Prescher, V. B. Prakapenka, S. Petitgirard, I. Chuvashova, B. Gasharova, Y.-L. Mathis, P. Ershov, I. Snigireva, and A. Snigirev, Sci. Adv. **2**, e1600341 (2016).
[35] S. M. Nikitin, N. Chigarev, V. Tournat, A. Bulou, D. Gasteau, B. Castagnede, A. Zerr, and V. E. Gusev, Sci. Rep. **5**, 9352 (2015).
[36] M. Kuriakose, S. Raetz, N. Chigarev, S. M. Nikitin, A. Bulou, D. Gasteau, V. Tournat, B. Castagnede, A. Zerr, and V. E. Gusev, Ultrasonics **69**, 259 (2016).
[37] R. Boehler, Rev. Sci. Instrum. **77**, 115103 (2006).
[38] F. A. Jenkins and H. E. White, *Fundamentals of Optics* (McGraw-Hill, New York, 1957), p. 265.
[39] H.-K. Mao, J. Xu, and P. M. Bell, J. Geophys. Res. **91**, 4673 (1986).
[40] C. Thomsen, H. T. Grahn, H. J. Maris, and J. Tauc, Phys. Rev. B **34**, 4129 (1986).
[41] M. Kuriakose, N. Chigarev, S. Raetz, A. Bulou, V. Tournat, A. Zerr, and V. E. Gusev, New J. Phys. **19**, 053026 (2017).
[42] Y.-W. Liu, in *Fourier Transform Applications*, edited by S. Salih (InTech, Shanghai, 2012), p. 291.
[43] P. Flandrin, *Time-Frequency/Time-Scale Analysis* (Academic Press, San Diego, 1999).
[44] M. Min, T. Parve, and A. Ronk, IEEE Trans. Instrum. Meas. **41**, 50 (1992).
[45] D. C. Rife and R. R. Boorstyn, IEEE Trans. Inf. Theory IT **20**, 591 (1974).
[46] W. A. Bassett, J. Phys.: Condens. Matter **18**, S921 (2006).
[47] M. Eremets, *High Pressure Experimental Methods* (Oxford University Press, Oxford, 1996).
[48] S. Merkel, C. Tome, and H. R. Wenk, Phys. Rev. B **79**, 064110 (2009).
[49] S. Merkel (private communication).
[50] C. Nisr, G. Ribárik, T. Ungár, G. B. M. Vaughan, P. Cordier, and S. Merkel, J. Geophys. Res. **117**, B03201 (2012).
[51] S. I. Karato, Phys. Rev. B **79**, 214106 (2009).
[52] G. Kresse and J. Hafner, Phys. Rev. B **47**, 558 (1993).
[53] G. Kresse and J. Hafner, Phys. Rev. B **48**, 13115 (1993).
[54] G. Kresse and J. Furthmuller, Phys. Rev. B **54**, 11169 (1996).
[55] J. P. Perdew, K. Burke, and M. Ernzerhof, Phys. Rev. Lett. **77**, 3865 (1996).
[56] P. E. Blochl, Phys. Rev. B **50**, 17953 (1994).
[57] G. Kresse and D. Joubert, Phys. Rev. B **59**, 1758 (1999).
[58] L. Verlet, Phys. Rev. **159**, 98 (1967).
[59] M. Born, Math. Proc. Cambridge Philos. Soc. **36**, 160 (1940).
[60] G. Grimvall, B. Magyari-Kope, V. Ozolins, and K. A. Persson, Rev. Mod. Phys. **84**, 945 (2012).
[61] D. Dzivenko, A. Zerr, N. Guignot, M. Mezouar, and R. Riedel, Europhys. Lett. **92**, 66001 (2010).
[62] D. M. Teter, MRS Bull. **23**, 22 (1998).
[63] S. F. Pugh, Philos. Mag. **45**, 823 (1954).
[64] D. G. Pettifor, Mater. Sci. Technol. **8**, 345 (1992).
[65] M. Yokoo, N. Kawai, K. G. Nakamura, K.-i. Kondo, Y. Tange, and T. Tsuchiya, Phys. Rev. B **80**, 104114 (2009).
[66] Y. Akahama and H. Kawamura, J. Phys.: Conf. Ser. **215**, 012195 (2010).